

Phase Evolution of a Prenucleator for Fast Li Nucleation in All-Solid-State Lithium Batteries

Xiaofei Yang, Xuejie Gao, Sankha Mukherjee, Kieran Doyle-Davis, Jiamin Fu, Weihan Li, Qian Sun, Feipeng Zhao, Ming Jiang, Yongfeng Hu, Huan Huang, Li Zhang, Shigang Lu, Ruying Li, Tsun-Kong Sham, Chandra Veer Singh,* and Xueliang Sun*

Undesirable Li dendrite growth under high current densities due to the nonuniform Li nucleation and growth has significantly hindered the development of high-rate all-solid-state lithium batteries (ASSLBs). Herein, the phase evolution of a Li prenucleator (MoS_2) is shown in working ASSLBs that renders a highly active nucleator (Mo), where Mo promotes fast Li nucleation and Li dendrite suppression. During plating, Li shows strong affinity with Mo, which guides Li fast nucleating and selectively depositing on Mo surface with a large specific surface, thus reducing the local current density. Moreover, a fast diffusion of Li atom on Mo (110) surface promotes uniform Li deposition and limits the Li dendrite growth. Benefitting from the reduced local current density as well as the improved Li dendrite suppression, Li–Li symmetric cells within MoS_2 prenucleator demonstrate excellent electrochemical performance, achieving cycle lifetimes as high as 1000 h for $1 \text{ mA cm}^{-2}/1 \text{ mAh cm}^{-2}$ and 780 h for $0.5 \text{ mA cm}^{-2}/2 \text{ mAh cm}^{-2}$. Additionally, developed Li-LFP ASSLBs demonstrate high capacity retention of 78% with an ultra-long cycling life of 3000 cycles under a high current density of 1 mA cm^{-2} . The general concept has the potential to be extended to other metal-sulfide prenucleators.

1. Introduction

All-solid-state lithium-metal batteries (ASSLBs) using solid-state electrolytes (SSEs) have received extensive attention as the next step beyond state-of-the-art Li-ion batteries, due to their improved safety and energy density.^[1] Among various SSEs, solid polymer electrolytes (SPEs) show promising properties such as high flexibility, easy fabrication, low cost/density, and high electrochemical/chemical stability, which make them one of the most promising candidates for practical application in the near future.^[2] However, the low operating current density, resulting in a relatively long battery charging time, is considered as one of the biggest hurdles in the development of SPE-based ASSLBs. Undesirable Li dendrite growth under high current densities due to the nonuniform Li nucleation is one of the critical issues facing the widespread adoption of these systems.

In recent years, tremendous efforts such as the introduction of high modulus inorganic fillers^[3] and the development of functional electrolyte additives^[4] have been focused on solving the Li dendrite issues. The former aims to enhance the mechanical strength of SPEs, while the latter to inhibit Li dendrite formation via Li/SPE interface modification. For instance, Zhang's group developed a $\text{Li}_{6.75}\text{La}_3\text{Zr}_{1.75}\text{Ta}_{0.25}\text{O}_{12}$ (LLZTO)-poly(ethylene oxide) (PEO) SPE and showed that LLZTO fillers can significantly improve the mechanical strength, thus ensuring Li–Li symmetric cells with long cycling life of over 400 h at 0.1 mA cm^{-2} .^[3e] Very recently, we proposed a PEO electrolyte-infused commercial 3D glass fiber scaffold and achieved excellent cycling stability for over 2000 h at a current density of 0.2 mA cm^{-2} (capacity: 0.2 mAh cm^{-2}).^[3f] Besides the enhancement of SPEs mechanical strength, Li/SPE interface modification via electrolyte additives has also shown positive effects in suppressing the Li dendrite growth. For instance, Armand's group proposed a LiN_3 as an electrolyte additive to induce the formation of a Li_3N protection layer on the surface of the Li anode. The results showed that Li–Li symmetric cells with LiN_3 additive can stably run for over 650 h at 0.1 mA cm^{-2} (capacity: 0.2 mAh cm^{-2}), which is over six times longer compared with the LiN_3 -free counterpart.^[4a] Despite this progress, it should be noted that most of the Li–Li symmetric cells and full batteries

Dr. X. Yang, X. Gao, K. Doyle-Davis, J. Fu, Dr. W. Li, Dr. Q. Sun, F. Zhao, R. Li, Prof. X. Sun
Department of Mechanical and Materials Engineering
University of Western Ontario
London, Ontario N6A 5B9, Canada
E-mail: xsun9@uwo.ca


X. Gao, J. Fu, Prof. T.-K. Sham
Department of Chemistry
University of Western Ontario
London, Ontario N6A 5B9, Canada

Dr. S. Mukherjee, M. Jiang, Prof. C. V. Singh
Department of Materials Science and Engineering
University of Toronto
Toronto, Ontario M5S 3E4, Canada
E-mail: chandraveer.singh@utoronto.ca

Dr. Y. Hu
Canadian Light Source
44 Innovation Boulevard, Saskatoon, Saskatchewan S7N 2V3, Canada

Dr. H. Huang
Glabat Solid-State Battery Inc.
700 Collip Circle, London, Ontario N6G 4X8, Canada

Dr. L. Zhang, Dr. S. Lu
China Automotive Battery Research Institute
Beijing 100088, P. R. China

 The ORCID identification number(s) for the author(s) of this article can be found under <https://doi.org/10.1002/aenm.202001191>.

DOI: 10.1002/aenm.202001191

are tested with low current density (typically $<0.5 \text{ mA cm}^{-2}$) based on Li foil with limited Li deposition surface, which cannot meet the practical requirements of ASSLBs. Further enhancing the operating current density of both Li–Li symmetric cells and full cells to realize high-rate ASSLBs is still challenging.

Herein, a prenucleator (MoS_2) is proposed to guide uniform lithium nucleation as well as selective Li depositions sites, thus leading to reduced local current density and improved Li dendrite suppression capability. Li–Li symmetric cells with the prenucleator demonstrated long cycling stability of over 1000 and 780 h under high current densities and areal capacities of $1 \text{ mA cm}^{-2}/1 \text{ mAh cm}^{-2}$ and $0.5 \text{ mA cm}^{-2}/2 \text{ mAh cm}^{-2}$, respectively. In contrast, the occurrence of short-circuiting is observed in the MoS_2 -free Li–Li symmetric cells after 25 h. Furthermore, the evolution of MoS_2 under the high reductive environment is revealed by combining synchrotron-based X-ray absorption near edge structure (XANES) and density functional theory (DFT) calculations. It is found that the MoS_2 is reduced to true nucleator (Mo) and Li_2S at the beginning of Li plating, where Mo shows high affinity with Li, thus leading to Li uniform nucleation and selective deposition. This observation is further supported by the DFT calculations. The results prove that Li shows higher adsorption energy and lower energy barrier on the surface of Mo (110), promoting the uniform Li deposition and suppressing Li dendrite growth. Benefitting from the reduced local current density and enhanced Li dendrite suppression capability, Li-LFP full cells delivered high capacity retention of 78% with an ultra-long cycling life of 3000 cycles under a high current density of 1 mA cm^{-2} (corresponding to a C-rate of 2 C). Insights gained from this work will open up new opportunities for the development of high-rate ASSLBs.

2. Result and Discussion

The MoS_2 prenucleator is grown on a carbon paper (CP), which acts as an interlayer between the SPE and Li anode (labeled as CP@MoS_2). Before MoS_2 growth, the CP fibers present a smooth surface with a diameter of around $10 \mu\text{m}$ according to the scanning electron microscopy (SEM) images shown in Figure S1 in the Supporting Information. After MoS_2 growth, a thin layer of MoS_2 nanosheets, according to the X-ray diffraction (XRD) results and SEM images exhibited in Figures S2 and S3 in the Supporting Information, is anchored on the surface of the CP.^[5] The elemental mappings and high resolution transmission electron microscopy (TEM) images with a lattice distance of 0.62 nm , belonging to MoS_2 (002) plane, further confirming the successfully grown MoS_2 (Figure S4, Supporting Information).^[6] Compared with bare Li foil, where Li preferably deposits in dendritic morphology, under high current densities/areal capacities, due to nonuniform Li flux (Figure 1a).^[7] The introduction of MoS_2 prenucleator possesses several merits shown in Figure 1b. First, the CP provides an integrated electron transport network for fast electron transfer. Moreover, the MoS_2 sheets can not only promote uniform Li nucleation but also supply a large surface for Li accommodation as well as reducing local current density. More importantly, the Li shows a lower diffusion barrier and fast diffusion rate on the surface of MoS_2 and its derivations, significantly inhibiting Li dendrite formation during the plating process.^[8] In this regard, such a multifunctional prenucleator is beneficial for suppressing Li dendrite under elevated operating current densities and areal capacities (Figure 1b).^[8a] To evaluate the performance of the prenucleator in ASSLBs, a poly(ethylene glycol) dimethyl ether (PEGDME) electrolyte infused into a

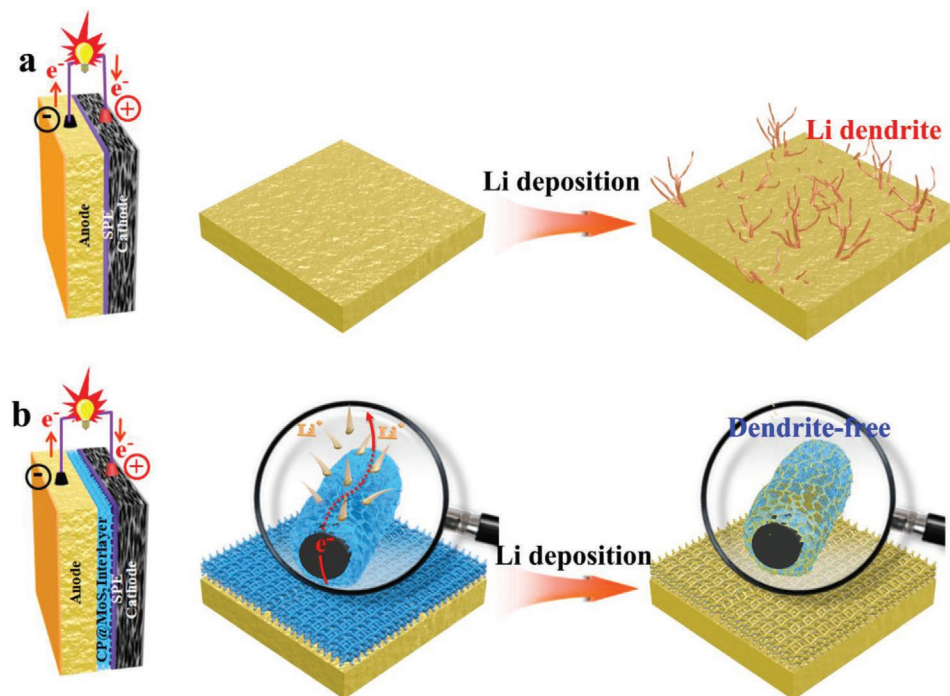


Figure 1. Schematic illustration of the Li deposition process in the ASSLBs a) without and b) with MoS_2 prenucleator.

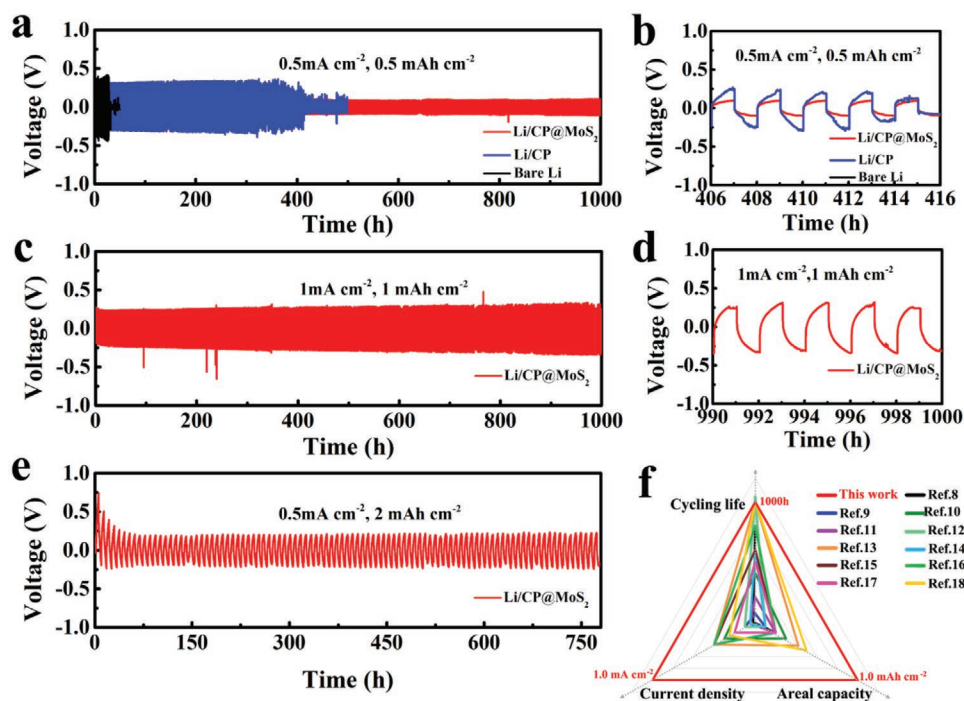


Figure 2. a) Cycling performance and b) plating/stripping profiles of the Li–Li symmetrical cells assembled with bare Li, Li/CP, and Li/CP@MoS₂ anodes at a current density of 0.5 mA cm⁻² (capacity: 0.5 mAh cm⁻²). c) Cycling performance and d) plating/stripping profiles of the Li–Li symmetrical cell assembled with Li/CP@MoS₂ anode at a current density of 1 mA cm⁻² (capacity: 1 mAh cm⁻²). e) Cycling performance of the Li–Li symmetrical cell assembled with Li/CP@MoS₂ anode at a current density of 0.5 mA cm⁻² (capacity: 2 mAh cm⁻²). f) Comparison of the recently reported plating/stripping performances of SPEs-based Li–Li symmetric cells with respect to current density, areal capacity, and cycling life (The reference number are coincided well with the references listed in Table S1 in the Supporting Information).

cellulose membrane (Figure S5, Supporting Information) is chosen as the electrolyte. Benefitting from the amorphous structure and stable structure of PEGDME (Figure S6, Supporting Information), the as-prepared SPE delivers a high ionic conductivity of 3.33×10^{-4} S cm⁻¹ at 60 °C (Figure S7a, Supporting Information) and an electrochemical stability window of 4.3 V (vs commercial C65 conductive carbon, Figure S7b, Supporting Information), which is suitable for evaluating the electrochemical performance of ASSLBs.

The role of the prenucleator in promoting uniform Li nucleation and accelerating selective Li deposition is evaluated by cycling assembled Li/CP@MoS₂ symmetrical cells at 60 °C. For comparison, the Li/CP and bare Li are chosen to assemble the Li–Li symmetrical cells and tested under the same conditions. As shown in **Figure 2a**, with a current density of 0.5 mA cm⁻² and an areal capacity of 0.5 mAh cm⁻², the Li/CP@MoS₂ cell presents a low initial overpotential of 169 mV, which is only 63% and 46% of the Li/CP (268 mV) and bare Li (364 mV) cells. The reduced overpotential of Li/CP@MoS₂ symmetric cell is further confirmed by the electrochemical impedance spectra (EIS) in Figure S8 in the Supporting Information. The semicircle at high frequency can be attributed to passivation layer impedance on Li metal surface (R_{SEI}), while the semicircle at low frequency is associated with the charge transfer resistance (R_{ct}) and the double layer capacitance at the electrolyte/Li interface.^[9] By fitting the spectra to the presented equivalent circuit, the R_{SEI} and R_{ct} of Li/CP@MoS₂ symmetric cells are 13.9 and 22.7 Ω cm⁻², which are much lower than those for the bare

Li (R_{SEI} : 48.1 Ω cm⁻², R_{ct} : 378.1 Ω cm⁻²) and Li/CP electrodes (R_{SEI} : 50.4 Ω cm⁻², R_{ct} : 164.2 Ω cm⁻²). The remarkably reduced R_{ct} can be attributed to the lithiophilicity and large specific surface area of MoS₂ prenucleator or its derivations that enhances Li deposition kinetics and electrode/electrolyte interface contact. It is expected to promote uniform Li nucleation and suppress Li dendrite growth. As the depth of Li plating/stripping increases, the overpotential of bare Li raises slightly to 423 mV after 25 h. Subsequently, the occurrence of a short-circuit is observed (Figure S9, Supporting Information), which can be attributed to nonuniform Li deposition on the bare Li and subsequent penetration into the SPE.^[3f,9c,10] Compared with bare Li, the cycling life of Li–Li symmetric cells within the CP is obviously improved. It can stably run for over 300 h with negligibly increased overpotential, suggesting its positive effect in suppressing Li dendrite. Nevertheless, unstable Li plating/stripping behavior and short-circuit appear after 415 h (Figure 2b). In other words, neither bare Li nor Li/CP is a suitable choice for pursuing dendrite-free ASSLBs, especially under high current densities/areal capacities. Interestingly, the Li–Li symmetric cells assembled with Li/CP@MoS₂ display remarkably improved cycling stability. According to our results, the Li–Li symmetric cells using Li/CP@MoS₂ can stably run for over 1000 h (Figure 2a) without significant overpotential growth (from 115 mV at 12 h to 118 mV at 1000 h confirmed by the EIS curve after cycling in Figure S10, Supporting Information), suggesting smooth Li plating and stripping during cycling. To further explore the potential application of prenucleator in

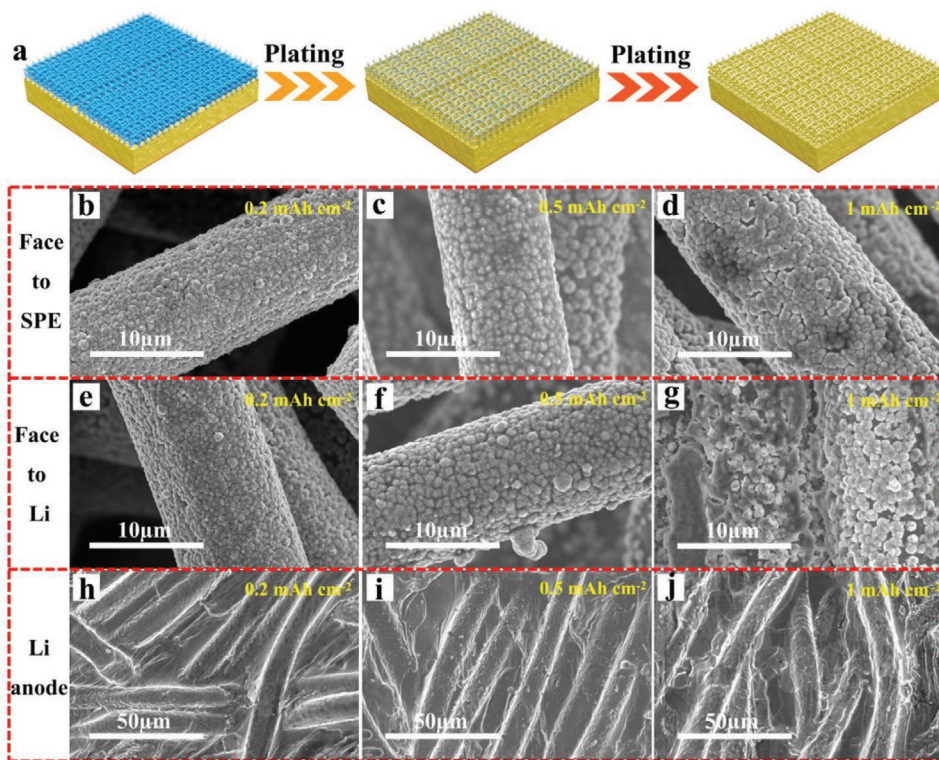


Figure 3. a) Schematic illustration of Li plating process on the Li/CP@MoS₂ anode. Surface SEM images of CP@MoS₂ closer to the SPE with Li plating capacities of b) 0.2, c) 0.5, and d) 1.0 mAh cm⁻². Surface SEM images of CP@MoS₂ closer to the Li anode with Li plating capacities of e) 0.2, f) 0.5, and g) 1.0 mAh cm⁻². Surface SEM images of Li anode with Li plating capacities of h) 0.2, i) 0.5, and j) 1.0 mAh cm⁻².

higher power/energy density ASSLBs, Li–Li symmetric cells are tested under elevated current densities/areal capacities of 1 mA cm⁻²/1 mAh cm⁻² and 0.5 mA cm⁻²/2 mAh cm⁻². Promisingly, these cells demonstrate excellent cycling performance for over 1000 and 780 h with low overpotentials of around 220 and 200 mV, respectively (Figure 2c–e). There is no doubt that such performance is superior to recently reported SPEs in terms of current density, areal capacity, and cycling life listed in Figure 2f and Table S1 in the Supporting Information.

To clarify the mechanism for the improved performance of the Li plating/stripping after the introduction of MoS₂ pre-nucleator, Li–Li symmetrical cells are cycled at 0.5 mA cm⁻² with different plating depths from 0.2 to 1.0 mAh cm⁻² are disassembled and the morphology of Li anode and CP@MoS₂ are inspected by SEM. Bare Li and Li/CP-based Li–Li symmetric cells are operated under the same conditions for comparison. As illustrated in Figure 3a, with the Li plating depth deeper, more Li deposits on the surface and gradually filled the MoS₂ sheets. As the SEM images displayed in Figure 3b,e and Figure S11a,d,g,j in the Supporting Information, with an areal capacity of 0.2 mAh cm⁻², both SPE side and Li anode side surface of MoS₂ sheets are filled with Li. Besides, some Li is also detected on the surface of Li anode (Figure 3h). This indicates that both MoS₂ and Li can act as active sites for Li deposition. It should be noted that Li anode side surface of MoS₂ sheets (Figure S11j, Supporting Information) contains more Li than the SPE side (Figure S11d, Supporting Information). This is further supported by the SEM images at larger

plating depths (Figure 3c,d,f,g and Figure S11b,c,e,f,h,i,k,l, Supporting Information). When the areal capacity is increased to 1 mAh cm⁻², some Li is observed to deposit in the gaps among the CP@MoS₂ fibers facing the Li anode, after the MoS₂ sheets are completely filled with Li (Figure 3g and Figure S11i,l, Supporting Information). By contrast, no residual Li can be seen in the gaps faced to the SPE (Figure 3c and Figure S11c,f, Supporting Information). With this in mind, we can conclude that the designed CP@MoS₂ interlayer can act as a 3D scaffold to provide abundant active sites to reduce the local current density and promote uniform Li nucleation.^[11] Moreover, after the MoS₂ sheets are filled with Li, Li preferentially deposits on the anode side surface of CP@MoS₂ fibers from bottom to top, which is also expected to reduce the risk of Li penetrating the SPE. The relevant SEM images of the CP and coupled Li anode are shown in Figure S12 in the Supporting Information. Due to the lithiophobicity of CP, which shows a higher Li deposition barrier compared with Li, where Li is preferred to deposit on the surface of Li anode.^[12] As can be seen, no Li is detected on both sides of the CP (Figure S12a–f, Supporting Information). Instead, an increasing amount of Li is found on the Li anode surface with the increasing Li plating depth (Figure S12g–i, Supporting Information). In this regard, the CP acts as a physical separator enlarging the distance required for dendrite growth. For the bare Li anode, due to the nonuniform Li deposition under high current densities (Figure S13, Supporting Information), Li dendrites can easily penetrate the SPE (Figure S13g–i, Supporting Information), leading to short-circuits.

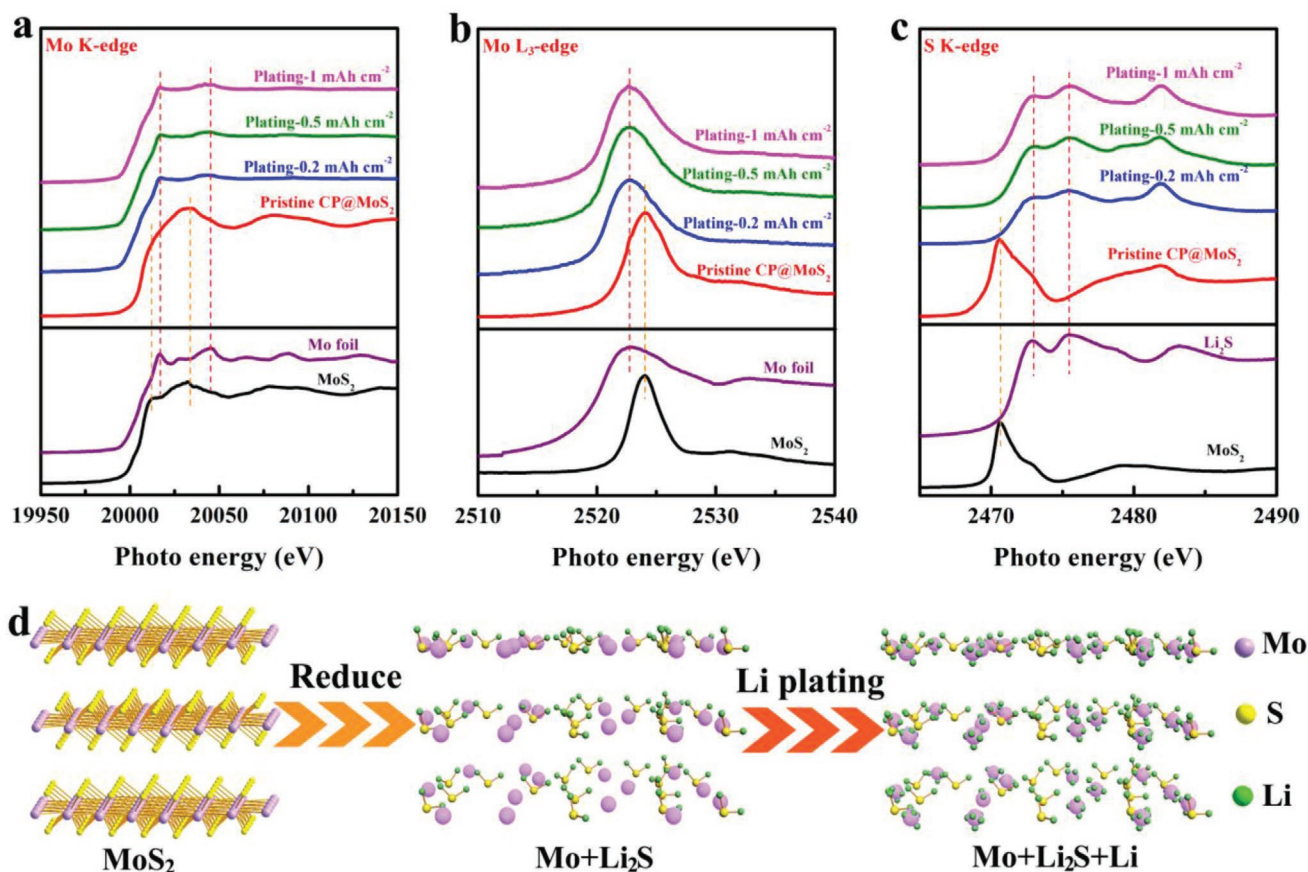


Figure 4. a) Mo K-edge, b) Mo L₃-edge, and c) S K-edge XANES of CP@MoS₂ at different depths of Li plating. d) Schematic illustration of MoS₂ evolution and Li deposition process.

Similarly, the surface morphology of the bare Li, Li/CP, and Li/CP@MoS₂ anodes is checked by SEM after 100, 500, and 1000 h under a current density of 0.5 mA cm⁻² (areal capacity: 0.5 mAh cm⁻²). As displayed in Figure S14 in the Supporting Information, for the bare Li, due to the nonuniform Li deposition under high current densities, a mossy Li layer with a thickness of 45 μm is detected on the Li surface. For the Li/CP anode, as shown in Figure S15 in the Supporting Information, due to the low Li diffusion on the Li/CP interface, the deposited Li grows as long dendrites and fully penetrates the CP paper. Some dendrites can be seen on the SPE side surface of CP, indicating that the lithiophobic conductive CP is inefficient in suppressing Li dendrite growth in ASSLBs. Promisingly, uniform Li deposition and no Li dendrite are observed on the CP@MoS₂ fibers (Figure S16, Supporting Information), even after 1000 h plating/stripping, further confirming the merits of MoS₂ pre-nucleator in inhibiting Li dendrite growth under high operating current densities and areal capacities. Based on the SEM images, we can conclude that the as-designed MoS₂ pre-nucleator can promote uniform Li nucleation as well as provide large space for Li deposition and accommodation, thus reducing local current density and suppressing Li dendrite.

To elucidate the underlying mechanism behind the selective deposition within MoS₂ pre-nucleator, synchrotron-based XANES measurements are used to identify the evolution of the

MoS₂ during plating. The Mo K-edge, Mo L₃-edge, and S K-edge XANES results are presented in Figure 4. Before Li plating, the Mo K-edge XANES of pristine CP@MoS₂, which arises from the Mo 1s to Mo 5p transition probing densities of states of Mo 5p character above the Fermi level in the band structure, is dominated by a broad resonance just above the edge jump, which is characteristic of MoS₂^[13] and is similar to that of MoS₂ nanosheets (Figure 4a).^[14] With the increase in the depth of plating, even at a low plating capacity of 0.2 mAh cm⁻², the edge jump and spectral feature generally shift to lower energy, as marked by the black vertical line, becoming very similar to the Mo K-edge XANES of Mo foil. This observation indicates that the reduction of MoS₂ to metallic Mo occurs during plating (Figure 4a). A similar shift to lower energy is also observed in the Mo L₃-edge XANES, in both the edge jump and the white-line maximum (Figure 4b), probing the Mo 4d_{5/2,3/2} unoccupied states in the conduction band above the Fermi level in MoS₂ and Mo, in the pristine and plated samples, respectively; this is accompanied by the broadening of the white-line and a reduction in the white-line intensity (Mo gains *d* charge upon reduction to Mo(0)). These observations indicate the transformation of MoS₂ to metallic Mo.^[15] It should also be noted that while the characteristic multiple scattering resonance at the Mo K-edge of the plated samples resemble those of Mo metal (red dash line), all feature are broadened, suggesting a noticeable reduction

in co-ordination numbers on average, a feature characteristic of nanostructures. The reduction of MoS₂ to Mo is confirmed by the S K-edge XANES (Figure 4c), the spectrum of pristine CP@MoS₂ is the same as that of MoS₂. With plating, we expect the formation of Li₂S through the MoS₂ reduction, which is confirmed by the S K-edge XANES.^[16] As we can clearly see from Figure 4c, the samples with Li plating exhibit an unmistakable XANES features of Li₂S. It is interesting to note that no energy shift or change in spectral features is observed in the Mo K-edge, Mo L₃-edge, or S K-edge XANES samples at higher plating capacities, suggesting that a stable chemical state is achieved after 0.2 mAh cm⁻² Li deposition, even after cycling for over 1000 h (Figure S17, Supporting Information). As such, we conclude that MoS₂ is reduced immediately by Li at the beginning of Li plating to form Mo and Li₂S which remain stable. The evolution process is further revealed by the TEM images shown in Figure S18 in the Supporting Information. As can be seen, the layered structure of MoS₂ is disappeared and some particles are dispersed in the structure. The particles show a lattice distance of 0.22 nm, which can be assigned to Mo (110) plane.^[17] Nevertheless, no crystal structure of Li₂S can be observed. By combining the XANES results and uniform distribution of elements of Mo and S (Figure S18d,e, Supporting Information), it can be speculated that Li₂S exists as the amorphous state.

To further clarify which component, Mo or Li₂S, is the true Li nucleator in promoting the selective deposition of Li during plating, Li–Li symmetric cells using Li/CP@MoS₂ anode are disassembled after standing for 24 h in a 60 °C oven. Interestingly, as shown in Figure S19 in the Supporting Information, after direct contact with Li for 24 h, the MoS₂ is directly reduced by Li and converted into Mo and Li₂S as evident from the Mo K-edge, Mo L₃-edge, and S K-edge XANES. The CP@MoS₂ contacted with Li for 24 h shows better Li affinity than the pristine CP@MoS₂. As shown in Figure S20 in the Supporting Information, the pristine CP@MoS₂ shows an initial lithiophobicity and almost no Li can be infused (Figure S20a, Supporting Information). Gradually, the lithiophobic surface becomes lithiophilic (Figure S20b,c, Supporting Information), which can be attributed to the reduction of MoS₂ to Mo and Li₂S. After 10 min, 80% of surface of the CP@MoS₂ is infused with Li (Figure S20c, Supporting Information). Interestingly, after contact with Li for 24 h, the surface of CP@MoS₂ is lithiophilic and the entire Li infusion process is shortened to 4 min (Figure S19d–f, Supporting Information). To further clarify whether Mo or Li₂S is lithiophilic, commercial Mo and Li₂S are chosen for the Li melting experiments. As shown in Figure S21 in the Supporting Information, it can be observed that Mo is the lithiophilic material, while the Li₂S is lithiophobic. Based on the analyses of XANES and Li melting experiments, as illustrated in Figure 4d, lithiophilic Mo derived from reduction of MoS₂ is the true Li nucleator inducing uniform Li nucleation and selective Li deposition.

To further confirm that lithiophilic Mo is the true Li nucleator that induces a uniform Li nucleation, we calculated adsorption energies, differential charge densities, and Li atom migration on the surfaces of graphene, MoS₂, and metallic Mo, using the DFT calculations. Details of the simulation parameters can be found in the Supporting Information. For layered graphene

and MoS₂, the Li atom diffusion path along with both armchair (ac) and zig-zag (zg) directions was investigated. For Mo metal, two most stable planes, Mo (110) and Mo (111) are chosen for adsorption energy and Li calculations. As shown in Figure 5d and Figure S22 in the Supporting Information, the adsorption energies (E_{Ad}) of Li on graphene, MoS₂, Mo (110), and Mo(111) are 0.07, -0.49, -0.98, and -1.30 eV, respectively. Differential charge density (DCD) plots shown in Figure 5a–c indicate that adsorbed Li atoms donate charge from its 1s orbital to the substrates. More negative values of E_{Ad} suggest stronger bonding between Li and the substrate, indicating that Li atoms interact strongly over Mo than MoS₂ and graphene.^[18] It can be used to interpret why Li preferentially and selectively deposit on the surface of MoS₂ prenucleator within the in situ formation of Mo nucleator during Li plating/stripping. Additionally, minimum energy pathways for a Li atom over graphene, MoS₂ and Mo surface and relevant energy profiles are summarized in Figure 5e–h and Figures S23 and S24 in the Supporting Information. Li diffusion energy barrier (E_a) over graphene along the ac and zg directions is similar, around 0.4 eV (by taking the energy difference between the initial and transition state). In the case of MoS₂, E_a along ac and zg directions are rather different, which are 0.82 and 0.28 eV, respectively. Following the Arrhenius equation, the diffusion constant is given by $D \propto \exp(-E_a/k_B T)$, where k_B is the Boltzmann constant, T is the operating temperature, and ν is a prefactor, which is an attempt frequency with values of the order of 10¹³ Hz. Using this equation, we arrive at the following prediction: Li preferentially diffuses along the zg direction and the energy barrier is around 0.12 eV lower than graphite. Therefore, Li diffusion over MoS₂ could be $\approx 10^2$ times faster than graphene at 300 K. Among the three substrates, the energy barrier on Mo (110) surface is the lowest, which is 0.17 eV. In other words, Li diffusion will be dominated by Li migration on the surface of Mo (110) with a much smaller energy barrier (0.17 eV) to overcome. Using the Arrhenius equation, diffusion of Li atom on Mo (110) is 73×10^3 times faster than graphene at 300 K. Therefore, the surface migration path accelerates the diffusion of Li to suppress Li dendrite growth. Based on the DFT calculations, as illustrated in Figure 5i, Li atom shows the highest absorption energy and lowest diffusion barrier on the surface of Mo, which results in Li atom selective deposition and fast diffusion on the surface of Mo, thus leading to the uniform deposition process.

The Li dendrite suppression and reduction in local current density of the MoS₂ prenucleator are further verified by Li-LFP ASSLBs (Figure 6a). The C-rate performance of Li-LFP ASSLBs using bare Li, Li/CP, and Li/CP@MoS₂ anode is first evaluated at galvanostatic charge/discharge C-rates from 0.2 C to 2 C (1 C = 170 mA g⁻¹), where LFP loading is controlled as 3 mg cm⁻². As displayed in Figure 6b, by reducing the local current density with the MoS₂ prenucleator, it reduces the Li deposition resistance (Figure S25, Supporting Information) and enables improved rate performance. At a rate of 0.5 C (equaling to a current density of around 0.25 mA cm⁻²), the Li/CP@MoS₂-LFP cell delivers a high capacity of 161 mAh g⁻¹ and a low overpotential of 0.28 V (Figure 6c). For comparison, the relative values for the Li/CP-LFP and Li-LFP cells are 153/142 mAh g⁻¹ and 0.37/0.46 V, respectively (Figure S26, Supporting Information). Further increasing the current density to

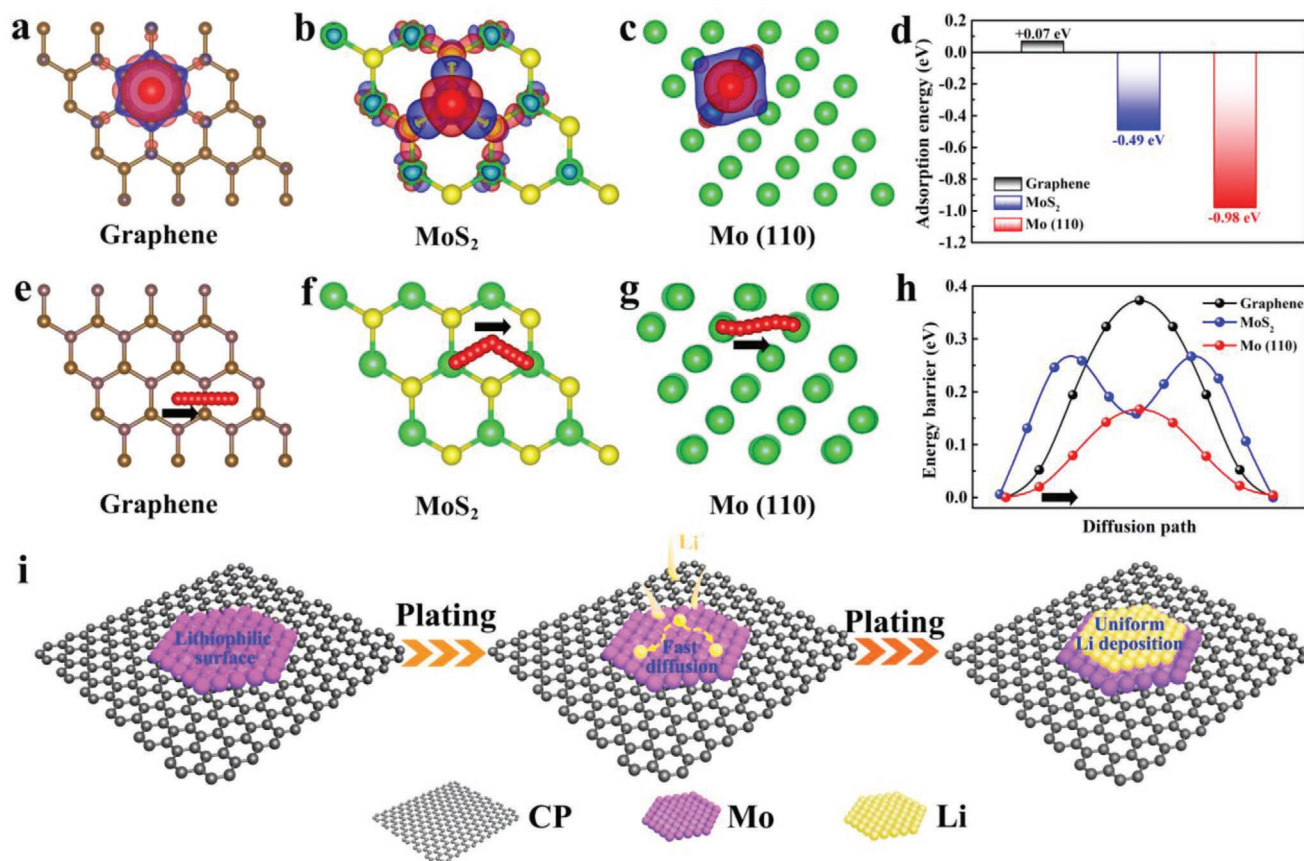


Figure 5. DCD between Li and a) graphene, b) MoS_2 , and c) Mo (110) surface. Color code for atoms: brown: C; red: Li; green: Mo; yellow: S. The iso-surface level for DCD plots is set to be $0.002 \text{ e} \text{ \AA}^{-3}$ wherein blue and red regions indicate charge accumulation and depletion, respectively. Minimum energy pathways for a Li atom over e) graphene, f) MoS_2 surface in the zigzag direction. g) Minimum energy pathway for a Li atom over Mo (110) surface. h) Associated energy profiles for Li atom diffusion. i) Schematic illustration of Li deposition process on the Mo surface during plating.

2 C, corresponding to a current density of around 1 mA cm^{-2} , the gap is further enlarged. The bare Li and Li/CP-based cells deliver capacities of $57/90 \text{ mAh g}^{-1}$, while the cell assembled with Li/CP@ MoS_2 anode still outputs a high capacity over 110 mAh g^{-1} . Moreover, it should be mentioned that a sharp drop in Coulombic efficiency (CE) is observed for the bare Li-based cell when the C-rates are higher than 0.8 C, suggesting the occurrence of short-circuiting and further confirmed by the charge–discharge profiles in Figure S26b in the Supporting Information.^[3f,19] By contrast, a similar phenomenon was not observed in the cells with Li/CP and Li/CP@ MoS_2 anodes, further demonstrating their positive impact. Generally speaking, the introduction of MoS_2 pre-nucleator is beneficial for enhancing the C-rate performance as well as reducing the risk of Li dendrite formation, which is of significance to pursue high power/energy density ASSLBs.

Besides the C-rate performance, the cycling life of the assembled cells is another critical parameter for batteries.^[20] The aforementioned three types of cells are further tested at 0.5 C for cycling stability evaluation. As shown in Figure 6d, similar to the C-rate performance testing, the cell using a bare Li anode presents a short-circuit followed by a sharp CE drop after 30 cycles, while the cell using Li/CP and Li/CP@ MoS_2 anodes maintain high CEs during long-term cycling of 200 cycles.

Compared with the Li/CP anode (152 mAh g^{-1} and 82%), the cell assembled with Li/CP@ MoS_2 anode exhibits higher capacity output (160 mAh g^{-1}) and capacity retention (95%). Considering the same cathode, SPE and testing conditions in the two cells, such a huge difference can be attributed solely to the presence of the MoS_2 pre-nucleator. Moreover, the long-term cycling performance of the Li/CP@ MoS_2 -LFP cell is also tested under a high C-rate of 2 C. As presented in Figure 6e,f, the cells exhibit excellent cycling stability with a high capacity retention of 78% after 3000 cycles, corresponding to an ultra-low capacity loss of 0.007% per cycle. The electrochemical performance of Li-LFP ASSLB using the Li/CP@ MoS_2 anode is superior to those recently reported in terms of current density and cycling life, listed in Figure 6g and Table S2 in the Supporting Information. Additionally, to achieve higher energy densities, Li/CP@ MoS_2 cell using a 6 mg cm^{-2} LFP-loaded cathode is investigated. As shown in Figure 6h, at a C-rate of 0.2 C, a high initial reversible capacity of around 150 mAh g^{-1} is delivered within 100 cycles, demonstrating excellent cycling stability.

3. Conclusion

In summary, we revealed the phase evolution of MoS_2 pre-nucleator in working ASSLBs that renders highly active Mo,

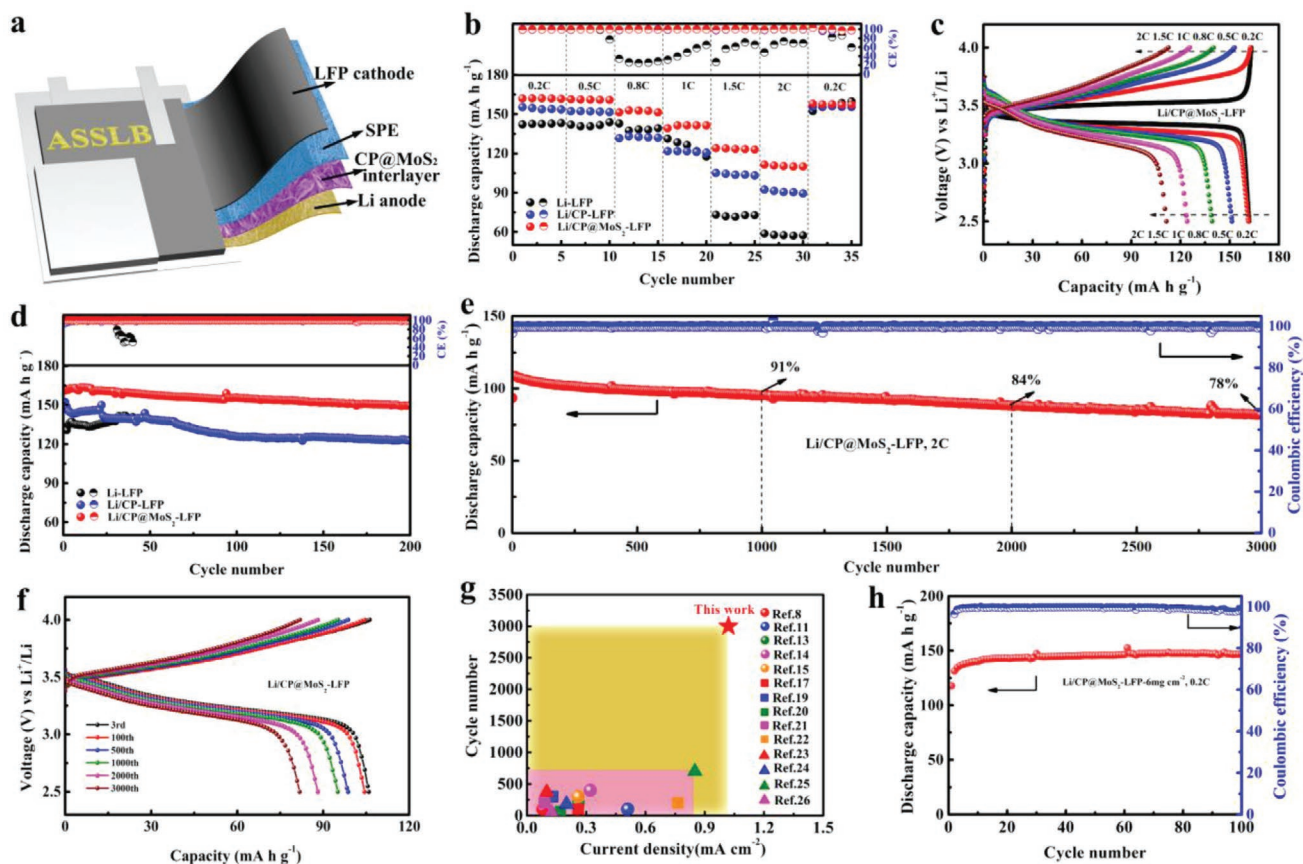


Figure 6. a) Schematic illustration of a Li/CP@MoS₂-LFP ASSEB. b) Rate performance of Li-LFP ASSEBs assembled with bare Li, Li/CP, and Li/CP@MoS₂ anodes tested at various C-rates from 0.2 C to 2 C and c) relative charge–discharge profiles of Li/CP@MoS₂-LFP cell. d) Cycling stability of Li-LFP ASSEBs assembled with bare Li, Li/CP, and Li/CP@MoS₂ anodes tested at 0.5 C. e) Long-term cycling stability of Li/CP@MoS₂-LFP cell tested at 2 C and f) relative charge–discharge profiles. g) Comparison of electrochemical performance in the terms of current density and cycling for Li/CP@MoS₂-LFP cell in this work with recent publications (The reference number are coincided well with the references listed in Table S2 in the Supporting Information). h) Cycling stability of the Li/CP@MoS₂-LFP cell assembled with a 6 mg cm⁻² LFP-loaded cathode at 0.2 C. (All of the cells are tested at an operating temperature of 60 °C).

where Mo is the true nucleator for fast Li nucleation and selective deposition. According to the XANES results and Li melting experiments, MoS₂ can be reduced to Mo at the beginning of Li plating. Mo nucleator facilitates uniform Li nucleation and offers a large volume for deposition and accommodation of Li, thus reducing the local current density and achieving dendrite-free Li deposition process under high current densities/areal capacities. This observation is further supported by DFT calculations, which show that Li exhibits strong adsorption energy (−0.98 eV) and a low diffusion barrier (0.17 eV) on Mo (110) surface. According to the Arrhenius equation, diffusion of Li atom on Mo (110) surface is 73 and 73 × 10³ times faster than MoS₂ and CP, respectively, which significantly inhibits the growth of Li dendrites and results into a smooth surface instead. As a result, the Li–Li symmetric cells assembled with Li/CP@MoS₂ anode demonstrate excellent Li plating/stripping performance, which stably runs for over 1000 and 780 h under current densities/areal capacities of 1 mA cm⁻²/1 mAh cm⁻² and 0.5 mA cm⁻²/2 mAh cm⁻², respectively. Benefitting from the smooth Li plating/stripping behavior, the assembled Li-LFP ASSEB delivers high capacity retention of 80% with an ultra-long cycling life of 3000 cycles under a high current density of 1 mA cm⁻². The general concept

has the potential to be extended to other metal-sulfide prenucleators.

Supporting Information

Supporting Information is available from the Wiley Online Library or from the author.

Acknowledgements

This work was partly supported by Natural Sciences and Engineering Research Council of Canada (NSERC), Canada Research Chair Program (CRC), Canada Foundation for Innovation (CFI), Ontario Research Fund, China Automotive Battery Research Institute Co., Ltd., Glabat Solid-State Battery Inc., and University of Western Ontario. C.V.S. acknowledges the additional support from Hart Professorship, Compute Canada, and University of Toronto. Q.S. appreciates the support of MITACS Elevate postdoctoral program. We also appreciate the help of the beamline scientists of SXRMB and HXMA beamlines at Canadian Light Source, Dr. Qunfeng Xiao, Dr. Mohsen Shakouri, Dr. Ning Chen, and Dr. Weifeng Chen.

Conflict of Interest

The authors declare no conflict of interest.

Author Contributions

X.Y. and X.G. contributed equally to this work. X.Y. and X.G. conceived and designed the experimental work and prepared the manuscript; X.G. helped with SEM characterization; K.D.-D. polished the manuscript; F.Z. helped with XRD characterization; J.F., W.L., Y.H., and T.-K.S. performed the XANES characterization and analyzed the XANES data; S.M., M.J., and C.V.S. designed and performed with DFT calculations and analysis; Q.S., L.Z., and S.L. participated in the discussion of the data; R.L. purchased all the chemicals; X.S. supervised the overall project. All authors have given approval to the final version of the manuscript.

Keywords

high rate, Li dendrite, solid polymer electrolyte, solid-state lithium batteries, uniform Li nucleation

Received: April 5, 2020

Revised: July 29, 2020

Published online: August 30, 2020

- [1] a) X. Yang, J. Luo, X. Sun, *Chem. Soc. Rev.* **2020**, *49*, 2140; b) A. Manthiram, X. Yu, S. Wang, *Nat. Rev. Mater.* **2017**, *2*, 16103; c) Y. Zhao, K. Zheng, X. Sun, *Joule* **2018**, *2*, 2583; d) Q. Zhou, J. Ma, S. Dong, X. Li, G. Cui, *Adv. Mater.* **2019**, *31*, 1902029; e) X. Yang, M. Jiang, X. Gao, D. Bao, Q. Sun, N. Holmes, H. Duan, S. Mukherjee, K. Adair, C. Zhao, J. Liang, W. Li, J. Li, Y. Liu, H. Huang, L. Zhang, S. Lu, Q. Lu, R. Li, C. V. Singh, X. Sun, *Energy Environ. Sci.* **2020**, *13*, 1318.
- [2] a) H. Zhang, J. Zhang, J. Ma, G. Xu, T. Dong, G. Cui, *Electrochem. Energy Rev.* **2019**, *2*, 128; b) J. Liang, J. Luo, Q. Sun, X. Yang, R. Li, X. Sun, *Energy Storage Mater.* **2019**, *21*, 308; c) S.-J. Tan, X.-X. Zeng, Q. Ma, X.-W. Wu, Y.-G. Guo, *Electrochem. Energy Rev.* **2018**, *1*, 113; d) J. Zhang, J. Yang, T. Dong, M. Zhang, J. Chai, S. Dong, T. Wu, X. Zhou, G. Cui, *Small* **2018**, *14*, 1800821; e) H. Huo, J. Sun, C. Chen, X. Meng, M. He, N. Zhao, X. Guo, *J. Power Sources* **2018**, *383*, 150; f) L. Liu, J. Lyu, J. Mo, H. Yan, L. Xu, P. Peng, J. Li, B. Jiang, L. Chu, M. Li, *Nano Energy* **2020**, *69*, 104398.
- [3] a) D. Lin, W. Liu, Y. Liu, H. R. Lee, P. C. Hsu, K. Liu, Y. Cui, *Nano Lett.* **2016**, *16*, 459; b) L. Chen, Y. Li, S.-P. Li, L.-Z. Fan, C.-W. Nan, J. B. Goodenough, *Nano Energy* **2018**, *46*, 176; c) X. Tao, Y. Liu, W. Liu, G. Zhou, J. Zhao, D. Lin, C. Zu, O. Sheng, W. Zhang, H. W. Lee, Y. Cui, *Nano Lett.* **2017**, *17*, 2967; d) H. Huo, Y. Chen, J. Luo, X. Yang, X. Guo, X. Sun, *Adv. Energy Mater.* **2019**, *9*, 1804004; e) C. Z. Zhao, X. Q. Zhang, X. B. Cheng, R. Zhang, R. Xu, P. Y. Chen, H. J. Peng, J. Q. Huang, Q. Zhang, *Proc. Natl. Acad. Sci. U. S. A.* **2017**, *114*, 11069; f) X. Yang, Q. Sun, C. Zhao, X. Gao, K. R. Adair, Y. Liu, J. Luo, X. Lin, J. Liang, H. Huang, L. Zhang, R. Yang, S. Lu, R. Li, X. Sun, *Nano Energy* **2019**, *61*, 567; g) L. Liu, L. Chu, B. Jiang, M. Li, *Solid State Ionics* **2019**, *331*, 89.
- [4] a) G. G. Eshetu, X. Judez, C. Li, O. Bondarchuk, L. M. Rodriguez-Martinez, H. Zhang, M. Armand, *Angew. Chem., Int. Ed.* **2017**, *56*, 15368; b) X. Yang, Q. Sun, C. Zhao, X. Gao, K. Adair, Y. Zhao, J. Luo, X. Lin, J. Liang, H. Huang, L. Zhang, S. Lu, R. Li, X. Sun, *Energy Storage Mater.* **2019**, *22*, 194.
- [5] a) P. T. Gomathi, P. Sahatiya, S. Badhulika, *Adv. Funct. Mater.* **2017**, *27*, 1701611; b) D. Qi, S. Li, Y. Chen, J. Huang, *J. Alloys Compd.* **2017**, *728*, 506.
- [6] a) C. Zhao, C. Yu, M. Zhang, Q. Sun, S. Li, M. Norouzi Banis, X. Han, Q. Dong, J. Yang, G. Wang, X. Sun, J. Qiu, *Nano Energy* **2017**, *41*, 66; b) X. Guo, Z. Wang, W. Zhu, H. Yang, *RSC Adv.* **2017**, *7*, 9009.
- [7] a) X.-B. Cheng, C.-Z. Zhao, Y.-X. Yao, H. Liu, Q. Zhang, *Chem* **2019**, *5*, 74; b) X. Zhang, S. Wang, C. Xue, C. Xin, Y. Lin, Y. Shen, L. Li, C. W. Nan, *Adv. Mater.* **2019**, *31*, 1806082.
- [8] a) E. Cha, M. D. Patel, J. Park, J. Hwang, V. Prasad, K. Cho, W. Choi, *Nat. Nanotechnol.* **2018**, *13*, 337; b) J. Hao, J. Zheng, F. Ling, Y. Chen, H. Jing, T. Zhou, L. Fang, M. Zhou, *Sci. Rep.* **2018**, *8*, 2079.
- [9] a) S. Xia, J. Lopez, C. Liang, Z. Zhang, Z. Bao, Y. Cui, W. Liu, *Adv. Sci.* **2019**, *6*, 1802353; b) T. Dong, J. Zhang, G. Xu, J. Chai, H. Du, L. Wang, H. Wen, X. Zang, A. Du, Q. Jia, X. Zhou, G. Cui, *Energy Environ. Sci.* **2018**, *11*, 1197; c) H. Huo, Y. Chen, N. Zhao, X. Lin, J. Luo, X. Yang, Y. Liu, X. Guo, X. Sun, *Nano Energy* **2019**, *61*, 119.
- [10] C. Wang, T. Wang, L. Wang, Z. Hu, Z. Cui, J. Li, S. Dong, X. Zhou, G. Cui, *Adv. Sci.* **2019**, *6*, 1901036.
- [11] a) J. Chen, B. Luo, Q. Chen, F. Li, Y. Guo, T. Wu, P. Peng, X. Qin, G. Wu, M. Cui, L. Liu, L. Chu, B. Jiang, Y. Li, X. Gong, Y. Chai, Y. Yang, Y. Chen, W. Huang, X. Liu, M. Li, *Adv. Mater.* **2020**, *32*, 1905578; b) Y. Zhao, X. Yang, L. Y. Kuo, P. Kaghazchi, Q. Sun, J. Liang, B. Wang, A. Lushington, R. Li, H. Zhang, X. Sun, *Small* **2018**, *14*, 1703717.
- [12] Y. Zhao, Q. Sun, X. Li, C. Wang, Y. Sun, K. R. Adair, R. Li, X. Sun, *Nano Energy* **2018**, *43*, 368.
- [13] B. Lassalle-Kaiser, D. Merki, H. Vrubel, S. Gul, V. K. Yachandra, X. Hu, J. Yano, *J. Am. Chem. Soc.* **2015**, *137*, 314.
- [14] D. Y. Chung, S. K. Park, Y. H. Chung, S. H. Yu, D. H. Lim, N. Jung, H. C. Ham, H. Y. Park, Y. Piao, S. J. Yoo, Y. E. Sung, *Nanoscale* **2014**, *6*, 2131.
- [15] K. P. C. Yao, M. Risch, S. Y. Sayed, Y.-L. Lee, J. R. Harding, A. Grimaud, N. Pour, Z. Xu, J. Zhou, A. Mansour, F. Bardé, Y. Shao-Horn, *Energy Environ. Sci.* **2015**, *8*, 2417.
- [16] a) X. Yang, X. Gao, Q. Sun, S. P. Jand, Y. Yu, Y. Zhao, X. Li, K. Adair, L. Y. Kuo, J. Rohrer, J. Liang, X. Lin, M. N. Banis, Y. Hu, H. Zhang, X. Li, R. Li, H. Zhang, P. Kaghazchi, T. K. Sham, X. Sun, *Adv. Mater.* **2019**, *31*, e1901220; b) X. Li, M. Banis, A. Lushington, X. Yang, Q. Sun, Y. Zhao, C. Liu, Q. Li, B. Wang, W. Xiao, C. Wang, M. Li, J. Liang, R. Li, Y. Hu, L. Goncharova, H. Zhang, T. K. Sham, X. Sun, *Nat. Commun.* **2018**, *9*, 4509; c) J. Fu, P. Yu, N. Zhang, G. Ren, S. Zheng, W. Huang, X. Long, H. Li, X. Liu, *Energy Environ. Sci.* **2019**, *12*, 1404.
- [17] X. Liu, D. Geng, X. Wang, S. Ma, H. Wang, D. Li, B. Li, W. Liu, Z. Zhang, *Chem. Commun.* **2010**, *46*, 6956.
- [18] X. Li, W. Zhang, J. Cai, H. Yan, M. Cui, G. Wu, M. Li, *Nano Energy* **2019**, *62*, 239.
- [19] X. Yang, X. Gao, C. Zhao, Q. Sun, Y. Zhao, K. Adair, J. Luo, X. Lin, J. Liang, H. Huang, L. Zhang, S. Lu, R. Li, X. Sun, *Energy Storage Mater.* **2020**, *27*, 198.
- [20] L. Liu, M. Li, L. Chu, B. Jiang, R. Lin, X. Zhu, G. Cao, *Prog. Mater. Sci.* **2020**, *111*, 100655.